

Commun. **7**, 1443 (1969).

⁷⁰J. G. Mavroides and B. Lax, Phys. Rev. **107**, 1530 (1957).

⁷¹O. N. Tufte and E. L. Stelzer, Phys. Rev. **141**, 675 (1966).

⁷²H. P. R. Frederikse, W. R. Hosler, and R. C. Casella, in *Proceedings of the Ninth International Conference on the Physics of Semiconductors*, edited by S. M. Ryukin (Nauka, Leningrad, 1968).

⁷³J. B. Goodenough, in Ref. 37.

⁷⁴W. H. Kleiner, J. Chem. Phys. **20**, 1784 (1952).

⁷⁵A. C. Switendick, MIT Solid-State and Molecular Theory Group Quarterly Progress Report No. 49, 1963 (unpublished).

⁷⁶T. E. Norwood and J. L. Fry, Phys. Rev. B **2**, 472 (1970).

⁷⁷See for example, J. M. Tyler, T. E. Norwood, and J. L. Fry, Phys. Rev. B **1**, 297 (1970).

⁷⁸L. Hodges, H. Ehrenreich, and D. N. Lang, Phys. Rev. **152**, 505 (1966); F. M. Mueller, *ibid.* **153**, 659 (1967).

⁷⁹K. Schwartz (private communication).

⁸⁰K. Schwartz, Monatsh. Chem. **102**, 1400 (1971).

⁸¹J. C. Slater, in *Computational Methods in Band Theory*, edited by P. M. Marcus, J. F. Janak, and A. R. Williams (Plenum, New York, 1971).

⁸²L. F. Mattheiss, Phys. Rev. B **5**, 315 (1972).

⁸³E. Šimánek and Z. Šroubek, Phys. Status Solidi **8**, K47 (1965).

⁸⁴W. B. Fowler, Phys. Rev. **151**, 657 (1966).

⁸⁵J. C. Slater and J. H. Wood, Intern. J. Quantum Chem. **4**, 3 (1971).

Effect of the 110°K Phase Transition on the SrTiO₃ Conduction Bands

L. F. Mattheiss

Bell Laboratories, Murray Hill, New Jersey 07974

(Received 26 May 1972)

The linear-combination-of-atomic-orbitals (LCAO) model of the preceding paper for the cubic-SrTiO₃ band structure is applied to predict the effect of the 110°K phase transition on the SrTiO₃ conduction bands. In this cubic-to-tetragonal structural transformation, neighboring octahedral TiO₆ complexes are rotated rigidly in opposite directions about the *c* axis through small angles $\pm\varphi$. This LCAO approach is expected to be accurate since nearest-neighbor distances and bond angles are unchanged in this transition. This enables one to apply the LCAO parameters for cubic SrTiO₃ to predict the band structure in the tetragonal state. The effects of the tetragonal distortion are introduced into the LCAO secular equation as small changes in the cubic structure factors, $e^{i\mathbf{k}\cdot\mathbf{R}_j}$. Neglecting spin-orbit coupling, this model predicts a splitting of the $\Gamma_{25'}$ conduction-band minimum by an energy proportional to φ^2 . At 4.2°K, where $c/a=1.0006$ and $\varphi=2.1^\circ$, $\Gamma_{25'}$ is split by about 90 meV into a lower doubly degenerate Γ_5+ state and an upper nondegenerate Γ_4+ state. Spin-orbit coupling further splits the Γ_5+ state by an energy comparable with the titanium 3*d* spin-orbit parameter, $\xi_{3d}\approx 25$ meV. This produces a warped single-valley model for the SrTiO₃ conduction bands at low carrier densities *n* and a two-band model containing "heavy" and "light" electrons for $n > 10^{19}$ cm⁻³. It is shown that the splitting of the conduction-band minimum in SrTiO₃ is similar in magnitude but opposite in sign to that caused by the ferroelectric transition in BaTiO₃.

I. INTRODUCTION

In the preceding paper¹ (hereafter referred to as I), the nonrelativistic augmented-plane-wave (APW) method has been combined with the linear-combination-of-atomic-orbitals (LCAO) interpolation scheme to determine the band structures for several "ideal" cubic perovskite-type compounds, including KNiF₃, SrTiO₃, KMoO₃, and KTaO₃. These calculations predict that the conduction-band minima for SrTiO₃ and KTaO₃ consist of warped bands at the zone center Γ rather than many valleys at or near the Brillouin-zone boundaries along the $\langle 100 \rangle$ directions, as Kahn and Leyendecker² have proposed. At the moment, there is no decisive experimental data for either compound that can distinguish between these warped-band

and many-valley models.

In the case of SrTiO₃, the interpretation of the low-temperature data is complicated by the occurrence of a cubic-to-tetragonal phase transition at about 110°K, plus the possibility of additional structural transformations at lower temperatures.³ Unoki and Sakudo⁴ have identified the space group of the tetragonal phase below 110°K as D_{4h}^{18} using electron-spin-resonance techniques. They find no evidence for a further reduction in symmetry down to 4.2°K. However, in a recent study involving monodomain samples, Sakudo and Unoki⁵ observe a dielectric anisotropy within the plane perpendicular to the *c* axis below 65°K, and this suggests that SrTiO₃ possesses orthorhombic or lower symmetry in this temperature range.

According to Lytle's x-ray data,³ the *c/a* ratio

in SrTiO_3 changes by only 6 parts in 10^4 between 110 and 4.2 °K. As a result, it has generally been assumed that the effect of the cubic-to-tetragonal phase transition on the SrTiO_3 band structure is negligible. However, there is some limited experimental evidence which indicates that the SrTiO_3 band structure is modified in the tetragonal state, particularly in the low-temperature piezoresistance,^{6,7} magnetoresistance,^{8,9} optical,¹⁰ and heat-capacity¹¹ data. Now that techniques for producing monodomain SrTiO_3 samples are available,¹² it is anticipated that detailed studies of the anisotropy in various physical properties will be investigated, effects that were previously obscured by the random alignment of domains at low temperatures.

The purpose of the present investigation is to apply the APW-LCAO model for the cubic SrTiO_3 band structure to predict the effect of the 110 °K cubic-to-tetragonal structural transformation on the SrTiO_3 conduction bands. This calculation is based entirely on the adjusted LCAO parameters for cubic SrTiO_3 . No additional parameters or adjustments are introduced in this study. The present investigation is concerned primarily with the effect of the cubic-to-tetragonal structural transformation on the titanium t_{2g} conduction-band states. It includes a simplified representation of the oxygen- $2p$ bands. It neglects the titanium- e_g and oxygen- $2s$ bands and all the nearest- and second-neighbor $2p$ - $2p$ valence-band interactions which are included in the cubic LCAO secular equation in I.

The present simplified LCAO model for tetragonal SrTiO_3 is described in Sec. II, along with the relevant information about the D_{4h}^{18} space group. This model is applied in Sec. III to obtain perturbation-theory estimates of the SrTiO_3 conduction-band splitting at the zone center and these results are compared with the analogous splittings which are produced by the ferroelectric transition in BaTiO_3 . The energy-band results for tetragonal SrTiO_3 are presented in Sec. IV, while the final section includes a discussion of these results and their implications regarding the electronic properties of monodomain SrTiO_3 at low temperatures, assuming that it remains tetragonal down to 4.2 °K.

II. LCAO MODEL FOR TETRAGONAL SrTiO_3

The relative positions of the individual atoms in cubic and tetragonal SrTiO_3 are compared in Figs. 1(a) and 1(b), respectively. The arrows in Fig. 1(b) indicate the directions in which the various oxygen atoms are displaced in the tetragonal state. The projection of one layer of titanium and oxygen atoms on the (001) plane is shown in Fig. 1(c). The dashed and broken lines in Fig. 1(c) indicate the boundaries of the Wigner-Seitz cell in

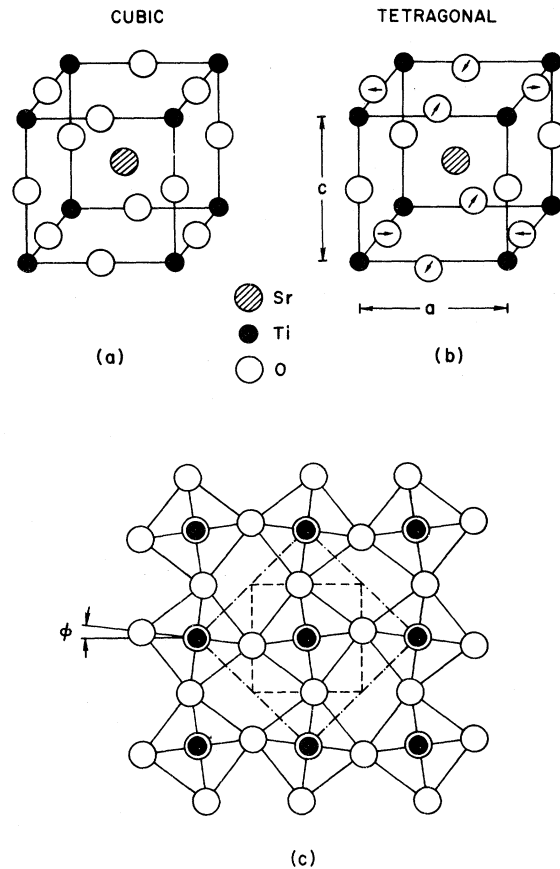


FIG. 1. (a) Atom positions in cubic SrTiO_3 . (b) Arrows indicate the displacement of the oxygen atoms in the tetragonal state. (c) The projection of one layer of titanium and oxygen atoms on a (001) plane.

the cubic and tetragonal phases, respectively. The angle ϕ is the angle between a nearest-neighbor titanium-oxygen bond in the (001) plane and the original cube axes. For a perfectly rigid rotation of neighboring TiO_6 octahedra, one expects that $c/a = 1/\cos\phi$, and, to within experimental error, this condition appears to be satisfied.^{3,4}

Unoki and Sakudo⁴ have shown that the space group for tetragonal SrTiO_3 is D_{4h}^{18} , which is a nonsymmorphic space group with a body-centered-tetragonal Bravais lattice. The primitive translations for this Bravais lattice are defined by the vectors

$$\begin{aligned} \vec{t}_1 &= \frac{1}{2}\sqrt{2} a(-\hat{i} + \hat{j}) + c\hat{k}, \\ \vec{t}_2 &= \frac{1}{2}\sqrt{2} a(\hat{i} - \hat{j}) + c\hat{k}, \\ \vec{t}_3 &= \frac{1}{2}\sqrt{2} a(\hat{i} + \hat{j}) - c\hat{k}, \end{aligned} \quad (1)$$

where \hat{i} , \hat{j} , and \hat{k} are unit vectors along the x , y , and z axes, respectively. Although the coordinate system that is represented by Eq. (1) is useful for constructing the symmetric Wigner-Seitz cell and

the corresponding Brillouin zone for the body-centered-tetragonal Bravais lattice (Fig. 2), we simplify the following discussion by describing the tetragonal state in terms of a pseudocubic coordinate system and the distortion angle φ .

According to Eq. (1), the volume of the tetragonal unit cell is $2a^2c$, or twice that of the cubic cell. As Koster¹³ points out, the body-centered-tetragonal Bravais lattice becomes fcc if $c = a$. This is very nearly the case in tetragonal SrTiO₃, where c/a increases to only 1.0006 between 110 and 4.2°K. Consequently, the Brillouin zone for the body-centered-tetragonal lattice with $c \approx a$ is very similar to that for the fcc lattice, as shown in Fig. 2.

It is interesting to note that two distinct space groups can be obtained by varying the stacking arrangement of the successive (001) layers which are shown in Fig. 1(c). According to Fig. 1(b), the D_{4h}^{18} space group is obtained if successive (001) layers are arranged so that neighboring TiO₆ complexes are rotated through opposite angles $\pm \varphi$ along the c axis. Another possible stacking arrangement has successive layers of Fig. 1(c) stacked one above the other, so that the rotation angle φ is identical for neighboring TiO₆ complexes along the c axis. In this case, the space group is D_{4h}^5 , the unit cell volume is again doubled, and the Bravais lattice is simple tetragonal.

The cubic-to-tetragonal phase transition from the O_h^1 to the D_{4h}^{18} space groups involves soft phonons at R . The doubling of the cubic unit cell causes the R point at the corner of the dashed cubic Brillouin zone in Fig. 2 to be folded onto the Γ point in the tetragonal state. These soft phonons have been observed directly in the Raman spectrum by Fleury *et al.*¹⁴ and in inelastic neu-

tron-scattering measurements.¹⁵ The corresponding transition from the O_h^1 to the D_{4h}^5 space group would involve soft phonons at M since, in this case, the doubling of the unit cell causes the M point to be folded into the Γ point in the tetragonal state. Apparently, there are no perovskite-type compounds which transform to this structure.

When the origin of coordinates is chosen at a titanium site, the symmetry operators $\{\alpha|\vec{t}\}$ for the space group D_{4h}^{18} are of two types. First, there are those operations whose rotational parts α correspond to the eight operations in the point group C_{4h} . These operations are always associated with primitive translations \vec{t} . The remaining operations in D_{4h}^{18} contain a combination of primitive translations plus the nonprimitive translation $\vec{\tau} = (0, 0, c)$. Since the present analysis is concerned only with the band structure for wave vectors within the body-centered-tetragonal Brillouin zone near $\vec{k} = 0$, we need not bother about the complications that can occur on the Brillouin-zone boundaries with nonsymmorphic space groups. Koster¹³ has shown that the appropriate irreducible representations for wave vectors inside the zone are just those for the corresponding point group.

The irreducible representations for the D_{4h} point group are tabulated by Koster.¹³ They include ten distinct representations, which we designate $\Gamma_{1\pm}, \Gamma_{2\pm}, \dots, \Gamma_{5\pm}$. Of these, eight are singly degenerate ($\Gamma_{1\pm}, \dots, \Gamma_{4\pm}$) and two are doubly degenerate ($\Gamma_{5\pm}$). It is easily shown that at the zone center, states which have $\Gamma_{25'}$ and $R_{25'}$ symmetry in the cubic state reduce to Γ_{4+}, Γ_{5+} and Γ_{3+}, Γ_{5+} in the tetragonal state, respectively. As a result, the tetragonal distortion is expected to reduce these cubic threefold degeneracies ($\Gamma_{25'}$ and $R_{25'}$) and produce a pair of doubly degenerate ($2\Gamma_{5+}$) and singly degenerate (Γ_{3+}, Γ_{4+}) bands at $\vec{k} = 0$. Along the c axis or Δ direction of Fig. 2, the group of the wave vector remains C_{4v} , as it was in the cubic case. However, in the basal plane, the corresponding groups along the $[100]$ (D) and $[110]$ (Σ) axes are reduced to C_{2v} . Finally, along the $[101]$ (S) and $[111]$ (Λ) axes, the appropriate point groups in the tetragonal state are C_s .

The LCAO matrix that is applied to determine the energy-band structure for tetragonal SrTiO₃ is summarized in Table I. A total of 16 oxygen- $2p$ and 6 titanium- $3d$ (t_{2g}) orbitals are involved in this simplified treatment. (The oxygen- $2p\sigma$ orbitals z_3 and z_6 are omitted, for reasons which are described below.) Since tetragonal SrTiO₃ retains its inversion symmetry, one can obtain a real LCAO matrix if the proper symmetrized combinations of LCAO basis functions are considered. These are defined in part B of Table I. In parts C and D, the various orbital energies and nonzero $3d-3d$ and $2p-3d$ energy-overlap integrals and

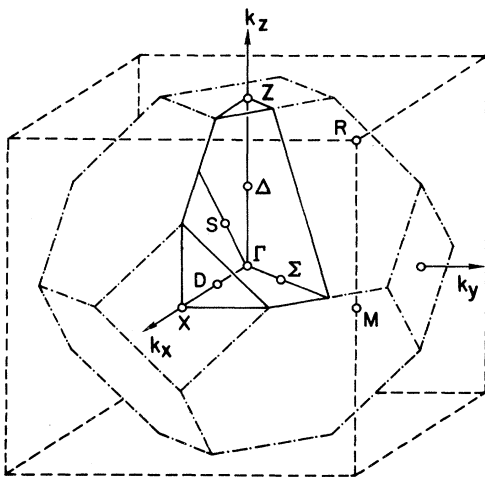


FIG. 2. Brillouin zone for the body-centered tetragonal Bravais lattice with $c \approx a$.

TABLE I. LCAO matrix for tetragonal SrTiO₃.

| Oxygen | | Titanium | | | |
|---|---|---|-------------------------|-----|--------------------------|
| Function | Origin | Function | Origin | | |
| A. Tight-binding orbitals | | | | | |
| x_1, y_1, z_1 | $a(\frac{1}{2}, -\frac{1}{2}\varphi, 0)$ | xy_1, yz_1, zx_1 | $a(0, 0, 0)$ | | |
| x_2, y_2, z_2 | $a(\frac{1}{2}\varphi, \frac{1}{2}, 0)$ | xy_2, yz_2, zx_2 | $a(1, 0, 0)$ | | |
| x_3, y_3 | $c(0, 0, \frac{1}{2})$ | | | | |
| x_4, y_4, z_4 | $a(-\frac{1}{2}, \frac{1}{2}\varphi, 0)$ | | | | |
| x_5, y_5, z_5 | $a(-\frac{1}{2}\varphi, -\frac{1}{2}, 0)$ | | | | |
| x_6, y_6 | $c(0, 0, -\frac{1}{2})$ | | | | |
| B. Basis functions | | | | | |
| No. | Symmetry | No. | Symmetry | No. | Symmetry |
| 1 | $(x_1 - x_4)/\sqrt{2}$ | 9 | $i(z_1 + z_4)/\sqrt{2}$ | 17 | $(xy_1 + xy_2)/\sqrt{2}$ |
| 2 | $(y_1 - y_4)/\sqrt{2}$ | 10 | $i(x_2 + x_5)/\sqrt{2}$ | 18 | $(xy_1 - xy_2)/\sqrt{2}$ |
| 3 | $(z_1 - z_4)/\sqrt{2}$ | 11 | $i(y_2 + y_5)/\sqrt{2}$ | 19 | $(yz_1 + yz_2)/\sqrt{2}$ |
| 4 | $(x_2 - x_5)/\sqrt{2}$ | 12 | $i(z_2 + z_5)/\sqrt{2}$ | 20 | $(yz_1 - yz_2)/\sqrt{2}$ |
| 5 | $(y_2 - y_5)/\sqrt{2}$ | 13 | $(x_3 - x_6)/\sqrt{2}$ | 21 | $(zx_1 + zx_2)/\sqrt{2}$ |
| 6 | $(z_2 - z_5)/\sqrt{2}$ | 14 | $(y_3 - y_6)/\sqrt{2}$ | 22 | $(zx_1 - zx_2)/\sqrt{2}$ |
| 7 | $i(x_1 + x_4)/\sqrt{2}$ | 15 | $i(x_3 + x_6)/\sqrt{2}$ | | |
| 8 | $i(y_1 + y_4)/\sqrt{2}$ | 16 | $i(y_3 + y_6)/\sqrt{2}$ | | |
| C. Diagonal matrix elements | | | | | |
| $H_{i,i} = E_{p\sigma}$ for $i = 1, 5, 7, 11$ | | $H_{19,19} = E_{d\pi} + 2(dd\delta)\cos\xi$ | | | |
| $H_{i,i} = E_{p\pi}$ for $i = 2-4, 6, 8-10, 12-16$ | | $H_{20,20} = E_{d\pi} - 2(dd\delta)\cos\xi$ | | | |
| $H_{17,17} = E_{d\pi} + 2(dd\delta)\cos\xi$ | | $H_{21,21} = E_{d\pi} + 2(dd\delta)\cos\eta$ | | | |
| $H_{18,18} = E_{d\pi} - 2(dd\delta)\cos\xi$ | | $H_{22,22} = E_{d\pi} - 2(dd\delta)\cos\eta$ | | | |
| D. Nonzero oxygen-titanium (p - d) energy (and overlap) interactions | | | | | |
| $h_1 \equiv 2E_{x,xy}(\frac{1}{2}, \frac{1}{2}\varphi, 0)$ | | $s_1 \equiv 2S_{x,xy}(\frac{1}{2}, \frac{1}{2}\varphi, 0)$ | | | |
| $h_2 \equiv 2E_{y,xy}(\frac{1}{2}, \frac{1}{2}\varphi, 0)$ | | $s_2 \equiv 2S_{y,xy}(\frac{1}{2}, \frac{1}{2}\varphi, 0)$ | | | |
| $h_3 \equiv 2E_{z,yz}(\frac{1}{2}, \frac{1}{2}\varphi, 0)$ | | $s_3 \equiv 2S_{z,yz}(\frac{1}{2}, \frac{1}{2}\varphi, 0)$ | | | |
| $h_4 \equiv 2E_{z,zx}(\frac{1}{2}, \frac{1}{2}\varphi, 0)$ | | $s_4 \equiv 2S_{z,zx}(\frac{1}{2}, \frac{1}{2}\varphi, 0)$ | | | |
| $h_5 \equiv 2E_{x,zx}(0, 0, \frac{1}{2})$ | | $s_5 \equiv 2S_{x,zx}(0, 0, \frac{1}{2})$ | | | |
| $H_{1,17} = h_1 \cos\frac{1}{2}\xi \cos\frac{1}{2}\varphi\eta$ | | $H_{7,17} = h_1 \cos\frac{1}{2}\xi \sin\frac{1}{2}\varphi\eta$ | | | |
| $H_{1,18} = h_1 \sin\frac{1}{2}\xi \sin\frac{1}{2}\varphi\eta$ | | $H_{7,18} = -h_1 \sin\frac{1}{2}\xi \cos\frac{1}{2}\varphi\eta$ | | | |
| $H_{2,17} = -h_2 \sin\frac{1}{2}\xi \sin\frac{1}{2}\varphi\eta$ | | $H_{8,17} = h_2 \sin\frac{1}{2}\xi \cos\frac{1}{2}\varphi\eta$ | | | |
| $H_{2,18} = -h_2 \cos\frac{1}{2}\xi \cos\frac{1}{2}\varphi\eta$ | | $H_{8,18} = -h_2 \cos\frac{1}{2}\xi \sin\frac{1}{2}\varphi\eta$ | | | |
| $H_{3,19} = h_3 \cos\frac{1}{2}\xi \cos\frac{1}{2}\varphi\eta$ | | $H_{9,19} = h_3 \cos\frac{1}{2}\xi \sin\frac{1}{2}\varphi\eta$ | | | |
| $H_{3,20} = h_3 \sin\frac{1}{2}\xi \sin\frac{1}{2}\varphi\eta$ | | $H_{9,20} = -h_3 \sin\frac{1}{2}\xi \cos\frac{1}{2}\varphi\eta$ | | | |
| $H_{3,21} = -h_4 \sin\frac{1}{2}\xi \sin\frac{1}{2}\varphi\eta$ | | $H_{9,21} = h_4 \sin\frac{1}{2}\xi \cos\frac{1}{2}\varphi\eta$ | | | |
| $H_{3,22} = -h_4 \cos\frac{1}{2}\xi \cos\frac{1}{2}\varphi\eta$ | | $H_{9,22} = -h_4 \cos\frac{1}{2}\xi \sin\frac{1}{2}\varphi\eta$ | | | |
| $H_{4,17} = h_2 \sin\frac{1}{2}\varphi\xi \sin\frac{1}{2}\eta$ | | $H_{10,17} = h_2 \cos\frac{1}{2}\varphi\xi \sin\frac{1}{2}\eta$ | | | |
| $H_{4,18} = -h_2 \cos\frac{1}{2}\varphi\xi \cos\frac{1}{2}\eta$ | | $H_{10,18} = h_2 \sin\frac{1}{2}\varphi\xi \cos\frac{1}{2}\eta$ | | | |
| $H_{5,17} = -h_1 \cos\frac{1}{2}\varphi\xi \cos\frac{1}{2}\eta$ | | $H_{11,17} = h_1 \sin\frac{1}{2}\varphi\xi \cos\frac{1}{2}\eta$ | | | |
| $H_{5,18} = h_1 \sin\frac{1}{2}\varphi\xi \sin\frac{1}{2}\eta$ | | $H_{11,18} = h_1 \cos\frac{1}{2}\varphi\xi \sin\frac{1}{2}\eta$ | | | |
| $H_{6,19} = h_4 \sin\frac{1}{2}\varphi\xi \sin\frac{1}{2}\eta$ | | $H_{12,19} = h_4 \cos\frac{1}{2}\varphi\xi \sin\frac{1}{2}\eta$ | | | |
| $H_{6,20} = -h_4 \cos\frac{1}{2}\varphi\xi \cos\frac{1}{2}\eta$ | | $H_{12,20} = h_4 \sin\frac{1}{2}\varphi\xi \cos\frac{1}{2}\eta$ | | | |
| $H_{6,21} = -h_3 \cos\frac{1}{2}\varphi\xi \cos\frac{1}{2}\eta$ | | $H_{12,21} = h_3 \sin\frac{1}{2}\varphi\xi \cos\frac{1}{2}\eta$ | | | |
| $H_{6,22} = h_3 \sin\frac{1}{2}\varphi\xi \sin\frac{1}{2}\eta$ | | $H_{12,22} = h_3 \cos\frac{1}{2}\varphi\xi \sin\frac{1}{2}\eta$ | | | |
| $H_{13,22} = -h_5 \cos\frac{1}{2}\xi$ | | $H_{15,21} = h_5 \sin\frac{1}{2}\xi$ | | | |
| $H_{14,20} = -h_5 \cos\frac{1}{2}\xi$ | | $H_{16,19} = h_5 \sin\frac{1}{2}\xi$ | | | |
| E. Two-center approximation for LCAO overlap and energy parameters | | | | | |
| $h_1 = 2 \sin\varphi [\sqrt{3} \cos^2\varphi (pd\sigma) + (1-2 \cos^2\varphi) (pd\pi)]$ | | $s_1 = 2 \sin\varphi [\sqrt{3} \cos^2\varphi S_\sigma + (1-2 \cos^2\varphi) S_\pi]$ | | | |
| $h_2 = 2 \cos\varphi [\sqrt{3} \sin^2\varphi (pd\sigma) + (1-2 \sin^2\varphi) (pd\pi)]$ | | $s_2 = 2 \cos\varphi [\sqrt{3} \sin^2\varphi S_\sigma + (1-2 \sin^2\varphi) S_\pi]$ | | | |
| $h_3 = 2(pd\pi)\sin\varphi$ | | $s_3 = 2S_\pi \sin\varphi$ | | | |
| $h_4 = 2(pd\pi)\cos\varphi$ | | $s_4 = 2S_\pi \cos\varphi$ | | | |
| $h_5 = 2(pd\pi)$ | | $s_5 = 2S_\pi$ | | | |

matrix elements are listed, with $\xi = k_x a$, $\eta = k_y a$, and $\zeta = k_z c$. In part D, only the energy matrix elements are tabulated explicitly. The corresponding

overlap matrix elements $S_{i,j}$ are easily obtained from $H_{i,j}$ by replacing the energy parameters h_k with the corresponding overlap parameters s_k .

The various LCAO energy (h_1-h_5) and overlap (s_1-s_5) parameters that occur in the tetragonal structure are related to the cubic LCAO parameters in part E, using the two-center approximation.

Several comments are in order concerning the approximations which are contained in this simplified LCAO model for tetragonal SrTiO₃. First, this model neglects both the nearest- and second-neighbor oxygen-oxygen $2p$ interactions that were included in the cubic LCAO matrix in I. In principle, the nearest-neighbor interactions could be included in this analysis since this distance is unchanged in the tetragonal state. However, it is quite tedious to work out in full detail the form of these matrix elements in the tetragonal state. The treatment of the second-neighbor interactions is more complicated since, according to Fig. 1, these distances vary with the rotation angle φ . As a result of these approximations, the present LCAO model does not provide any detailed information concerning the effect of the tetragonal distortion on the oxygen- $2p$ valence bands. It neglects the effects of valence-band dispersion on the shape of the conduction bands near $\vec{k}=0$.

It is easily shown that the matrix elements which connect the titanium- t_{2g} and the oxygen- z_3 and $-z_6$ orbitals vanish. As a result, these bands are perfectly flat (with energy equal to $E_{p\sigma}$) in both the cubic and tetragonal states when nearest-neighbor $2p-2p$ interactions are neglected. Consequently, these orbitals have been omitted from the LCAO matrices in Table I.

The energy-overlap parameters h_1, s_1 and h_2, s_2 of Table I, part E involve the two-center parameters $(pd\sigma)$, S_σ , $(pd\pi)$, and S_π . In the cubic perovskite structure, the parameters $(pd\pi)$ and S_π are determined from interactions involving the oxygen- $2p\pi$ and the titanium- t_{2g} orbitals whereas $(pd\sigma)$ and S_σ involve the $2p\sigma$ and e_g orbitals. Since the radial wave functions for the oxygen- $2p\sigma-2p\pi$ and titanium- e_g-t_{2g} orbitals are not necessarily identical in the perovskite structure, the parameters $(pd\sigma)$ and S_σ in Table I, part E may differ from those derived in I from the $e_g-2p\sigma$ interactions in cubic SrTiO₃. However, these differences are not expected to be substantial so that we shall apply the values for the $(pd\sigma)$ and S_σ parameters that are determined in I to the present study.

Finally, this LCAO model neglects the interaction between the oxygen- $2s$ and the titanium- t_{2g} orbitals in the tetragonal state. According to the analysis in I, these interactions vanish in the cubic state. However, using the values for $(sd\sigma)$ and S_s that are derived from the oxygen- $2s$ and titanium- e_g bands in the cubic state, we show in the following section that these interactions have a small effect on the states near the conduction-band minimum in tetragonal SrTiO₃.

III. ESTIMATES OF $\Gamma_{25'}$ SPLITTING IN TETRAGONAL SrTiO₃ AND BaTiO₃

Although one can solve the secular equation that is derived from the LCAO matrix of Table I exactly with the aid of a computer, it is useful to first estimate the magnitude of the splittings using second-order perturbation theory. In this section, we utilize this approach to compare the effects of the tetragonal distortion in SrTiO₃ and the ferroelectric transition in BaTiO₃ on the conduction-band minimum $\Gamma_{25'}$.

In tetragonal SrTiO₃ at $\vec{k}=0$, the off-diagonal $2p-3d$ energy (overlap) matrix elements involving the states which evolve from $\Gamma_{25'}$ are $\sqrt{2} h_1(\sqrt{2} s_1)$ and $h_3 (s_3)$, respectively. To second order, the energies of the conduction-band states with Γ_4+ and Γ_5+ symmetry are given by

$$E(\Gamma_4+) \approx E(\Gamma_{25'}) + 2(h_1 - E_{d\pi} s_1)^2 / (E_{d\pi} - E_{p\pi}), \quad (2a)$$

$$E(\Gamma_5+) \approx E(\Gamma_{25'}) + (h_3 - E_{d\pi} s_3)^2 / (E_{d\pi} - E_{p\pi}). \quad (2b)$$

According to the results of part E of Table I, these equations are equivalent to

$$E(\Gamma_4+) \approx E(\Gamma_{25'}) + 8 \sin^2 \varphi \frac{A^2}{E_{d\pi} - E_{p\pi}}, \quad (3a)$$

$$E(\Gamma_5+) \approx E(\Gamma_{25'}) + \frac{1}{2} \sin^2 \varphi \left(\frac{8[(pd\pi) - E_{d\pi} S_\pi]^2}{E_{d\pi} - E_{p\pi}} \right) \\ \approx E(\Gamma_{25'}) + \frac{1}{2} \sin^2 \varphi \Delta_\pi, \quad (3b)$$

where

$$A \equiv \sqrt{3} \cos^2 \varphi [(pd\sigma) - E_{d\pi} S_\sigma] \\ + (1 - 2 \cos^2 \varphi) [(pd\pi) - E_{d\pi} S_\pi]. \quad (4)$$

In Eq. (3b), the quantity in large parentheses on the right-hand side of the first line is replaced by Δ_π [Eq. (5) of I] in the second.

It is clear from Eq. (3) that both $E(\Gamma_4+)$ and $E(\Gamma_5+)$ reduce properly to $E(\Gamma_{25'})$ in the limit where the angle φ approaches zero. According to Eq. (3), $E(\Gamma_4+)$ and $E(\Gamma_5+)$ are each raised above $E(\Gamma_{25'})$ when the titanium- t_{2g} conduction bands are above the oxygen- $2p$ valence bands [$(E_{d\pi} - E_{p\pi}) > 0$], so that the actual splitting depends on the relative magnitude of the second terms on the right-hand side of Eq. (3). To evaluate these terms, we use the adjusted LCAO parameters for SrTiO₃ of I, which are listed in Table II. With energies expressed in electron volts, it is found that

$$E(\Gamma_4+) \approx E(\Gamma_{25'}) + 63 \sin^2 \varphi, \quad (5)$$

$$E(\Gamma_5+) \approx E(\Gamma_{25'}) + 1.7 \sin^2 \varphi.$$

Thus, the shift in $E(\Gamma_4+)$ is 40 times larger than that in $E(\Gamma_5+)$. In Sec. IV we show that the latter state represents the conduction-band minimum in tetragonal SrTiO₃. At 4.2 °K, where $\varphi = 2.1^\circ$, Eq. (5) predicts that

$$E(\Gamma_4+) \approx E(\Gamma_{25'}) + 0.085 \text{ eV},$$

TABLE II. LCAO parameters involved in the present simplified LCAO model for tetragonal SrTiO₃. Energies are in electron volts.

| Parameter | Fitted | Adjusted |
|---------------|---------|----------|
| $E_{p\sigma}$ | -0.8120 | -0.8120 |
| $E_{p\pi}$ | -1.0251 | -1.0251 |
| $E_{d\pi}$ | 6.3444 | 2.9931 |
| $(dd\delta)$ | -0.0167 | -0.0167 |
| S_{σ} | 0.0777 | 0.0777 |
| $(pd\sigma)$ | -2.1224 | -2.2526 |
| S_{π} | -0.0584 | -0.0584 |
| $(pd\pi)$ | 1.0374 | 1.1354 |
| ξ_{3d} | ... | 0.0245 |

$$E(\Gamma_5+) \approx E(\Gamma_{25'}) + 0.002 \text{ eV.} \quad (6)$$

The total splitting is therefore predicted to be about 80 meV.

We now estimate the effect of neglected 2s-3d interactions on this splitting. At $k=0$, the matrix elements connecting the 3d state with Γ_5+ symmetry vanishes. For the Γ_4+ state, the corresponding 2s-3d energy (overlap) matrix element is $2\sqrt{3} \sin\varphi \cos\varphi (sd\sigma)$ ($2\sqrt{3} \sin\varphi \cos\varphi S_s$). This contributes an additional term to $E(\Gamma_4+)$, which can be written as $2\sin^2\varphi \cos^2\varphi \Delta_s$, where Δ_s is also defined by Eq. (5) of I. According to the results of Table X in I, $\Delta_s \approx 2 \text{ eV}$ in cubic SrTiO₃, so that $2\sin^2\varphi \cos^2\varphi \Delta_s \approx 0.005 \text{ eV}$ at 4.2 °K, where $\varphi = 2.1^\circ$. This additional contribution to $E(\Gamma_4+)$ increases the total $E(\Gamma_4+) - E(\Gamma_5+)$ splitting to about 90 meV at 4.2 °K.

It is interesting to compare this splitting of the conduction-band minimum in tetragonal SrTiO₃ with that expected in ferroelectric BaTiO₃. Brews¹⁵ has applied the Kahn-Leyendecker² model for cubic SrTiO₃ to this problem and has shown that the $\Gamma_{25'}$ splitting in tetragonal BaTiO₃ is opposite to that predicted here for SrTiO₃. According to the results shown in Fig. 1 of Brews's paper, $\Gamma_{25'}$ is split in the ferroelectric state into a lower nondegenerate Δ_2' state and an upper doubly degenerate Δ_5 state. The total splitting is about 90 meV, which is remarkably similar to the present estimate of the analogous splitting in tetragonal SrTiO₃.

In order to determine the various contributions to this splitting in tetragonal BaTiO₃, we consider a simplified model of the ferroelectric transition in which all the atoms in the unit cell are fixed except the titanium atom. In the tetragonal state, the titanium atoms are displaced along the c axis by $\frac{1}{2}\epsilon a$, where $\epsilon \approx 0.056$.¹⁷ We now define φ as the angle which the displaced titanium atom makes with the (001) plane containing the four nearest-neighbor oxygen atoms. In terms of the observed titanium displacement, $\varphi = 3.1^\circ$ at 20 °C in BaTiO₃.

It is straightforward to work out the corresponding LCAO matrix for this case. Since the ferroelectric transition destroys inversion symmetry, the LCAO matrix can no longer be made real. Applying second-order perturbation theory at $k=0$, the energies of the Δ_2' and Δ_5 states are given by

$$E(\Delta_2') = E(\Gamma_{25'}) \quad , \quad (7a)$$

$$E(\Delta_5) \approx E(\Gamma_{25'}) + \frac{[h_1 - E_{d\pi} s_1]^2 + [h_3 - E_{d\pi} s_3]^2 + (\delta\pi)^2}{E_{d\pi} - E_{p\pi}} \quad (7b)$$

It is found that energy of the nondegenerate Δ_2' state is unchanged in the BaTiO₃ ferroelectric transition whereas $E(\Delta_5)$ is raised by three additional contributions. The first two contributions involve the same LCAO energy (overlap) parameters $h_1(s_1)$ and $h_3(s_3)$ that occur in the corresponding calculation for tetragonal SrTiO₃ [Eq. (2)]. The last term on the right-hand side of Eq. (7b) involves a new parameter, $\delta\pi$. This term arises from the fact that, in its displaced position, the titanium atom has moved closer to one oxygen atom along the c axis and further from the opposite one. This produces two different energy and overlap matrix elements, which we denote by $(pd\pi)^+$ and S_{π}^+ , respectively. It is easily shown that $\delta\pi$ is given by

$$\delta\pi = (pd\pi)^+ - (pd\pi)^- - E_{d\pi}(S_{\pi}^+ - S_{\pi}^-) \quad . \quad (8)$$

Using the results of Eqs. (2) and (5) and setting $\varphi = 3.1^\circ$, we estimate that the h_1 , s_1 and h_3 , s_3 contributions to $E(\Delta_5)$ in Eq. (7b) are about 0.094 eV.

To evaluate the $\delta\pi$ contribution to $E(\Delta_5)$, we must determine the distance dependence of $(pd\pi)$ and S_{π} . Zook and Casselman¹⁸ have estimated the dependence of S_{π} on the nearest-neighbor distance d , using atomic wave functions. Their results predict that for the observed displacements in BaTiO₃, the ratios $S_{\pi}^+/S_{\pi} = 0.84$ and $S_{\pi}^-/S_{\pi} = 1.19$, respectively. If we assume that the ratios $(pd\pi)^+/(pd\pi)$ and $(pd\pi)^-/(pd\pi)$ scale in the same way, the $\delta\pi$ contribution to $E(\Delta_5)$ can be written

$$\frac{1}{8}(S_{\pi}^+ - S_{\pi}^-/S_{\pi})^2 \Delta_{\pi} \quad ,$$

and this amounts to about 50 meV. Thus, the total splitting of the $\Gamma_{25'}$ state in ferroelectric BaTiO₃ is estimated to be about 150 meV at 20 °C. This result is in reasonable agreement with the 120 meV splitting that Berglund and Baer¹⁹ infer from measurements of the Seebeck-coefficient anisotropy.

The main source of the 60 meV discrepancy between the present estimate of the $\Gamma_{25'}$ splitting in ferroelectric BaTiO₃ and Brews's earlier calculation¹⁶ can be traced to the relative signs of the covalency integrals $(pd\sigma)$ and $(pd\pi)$. Brews's

calculation is based on the Kahn-Leyendecker² model for SrTiO₃, where $(pd\sigma)$ and $(pd\pi)$ are both positive. This causes the σ and π terms in A of Eq. (4) to cancel rather than add, thereby reducing the magnitude of this contribution to the total splitting. If the sign for $(pd\sigma)$ is changed, Brews's calculation yields a $\Delta_5 - \Delta_2$ splitting of 120 meV, which is precisely the experimental value quoted by Berglund and Baer.¹⁹

IV. RESULTS

We now consider in more detail the nature of the SrTiO₃ conduction bands near the minimum at $\vec{k}=0$. The results presented in this section are obtained by solving exactly the secular equation for tetragonal SrTiO₃ that is obtained from the energy and overlap matrices of Table I and the adjusted LCAO parameters of Table II. As in I, spin-orbit effects are introduced by means of a titanium- $3d$ spin-orbit parameter, $\xi_{3d}=0.025$ eV.

The splitting of the SrTiO₃ conduction-band minimum as a function of the rotation angle ϕ is shown in Fig. 3 with $\xi_{3d}=0$ and 0.025 eV. When spin-orbit coupling is neglected, the $\Gamma_{25'}$ state is split by the tetragonal distortion into a lower Γ_5+ and an upper Γ_4+ state. At 4.2°K, where $\phi=2.1^\circ$, the energy splitting between Γ_4+ and Γ_5+ is 87 meV, which is slightly greater than the perturbation-theory estimate of 83 meV in Eq. (6).

The corresponding pattern of splittings becomes more complex when spin-orbit coupling is included. In the cubic state where $\phi=0$, the $\Gamma_{25'}$ state is split by $\frac{3}{2}\xi_{3d}$, or 0.038 eV for $\xi_{3d}=0.025$ eV. This splitting preserves the center of gravity of the $\Gamma_{25'}$ state, since the energy of the fourfold degenerate Γ_8+ state is lowered by $\frac{1}{2}\xi_{3d}$ while that of the doubly degenerate Γ_7+ state is raised by ξ_{3d} . In the tetragonal state where $\phi \neq 0$, the Γ_8+

state is split into a pair of doubly degenerate states whose energies approach $E(\Gamma_5+) \pm \frac{1}{2}\xi_{3d}$ at large angles. Similarly, the energy of the doubly degenerate state which evolves from Γ_7+ approaches that of the Γ_4+ state when $\phi \sim 2^\circ$. For $\phi=2.1^\circ$, the splitting of the lower bands is about 20 meV and the total splitting is approximately 100 meV.

The energy-band results near $\vec{k}=0$ are shown in Fig. 4 with $\xi_{3d}=0$. In the tetragonal state, these results are shown for $\phi=0, 1^\circ$, and 2.1° and \vec{k} along the $[001]$ (Δ), $[100]$ (D), $[110]$ (Σ), $[101]$ (S), and $[111]$ (Λ) directions. The results in the first column are obtained from the cubic LCAO model for SrTiO₃ that is presented in I. By comparing these results with those derived from the present simplified model for tetragonal SrTiO₃ with $\phi=0$, one can determine the accuracy of the latter model near the conduction-band minimum. It is clear that the simplifications that are introduced in the present LCAO model for the tetragonal state have little effect on the accuracy of the bands in this energy range.

When $\phi \neq 0$, the most interesting results are those for wave vectors along the $[001]$ (Δ) and $[100]$ (D) directions. In the former case, the energy of the cubic Δ_5 band is essentially unchanged in the tetragonal state and the flat Δ_2 band is rigidly shifted with the Γ_4+ state, with no noticeable change in its width or shape. Along the $[100]$ or D direction, the flat cubic Δ_2 band becomes an equally flat D_4 band, while the center of gravity of the D_2 and D_3 bands tends to follow the cubic Δ_5 band. Similar changes occur in the tetragonal state for wave vectors along other symmetry directions.

The effect of including spin-orbit coupling in these calculations is shown in Fig. 5. As expected, this introduces additional splittings and eliminates

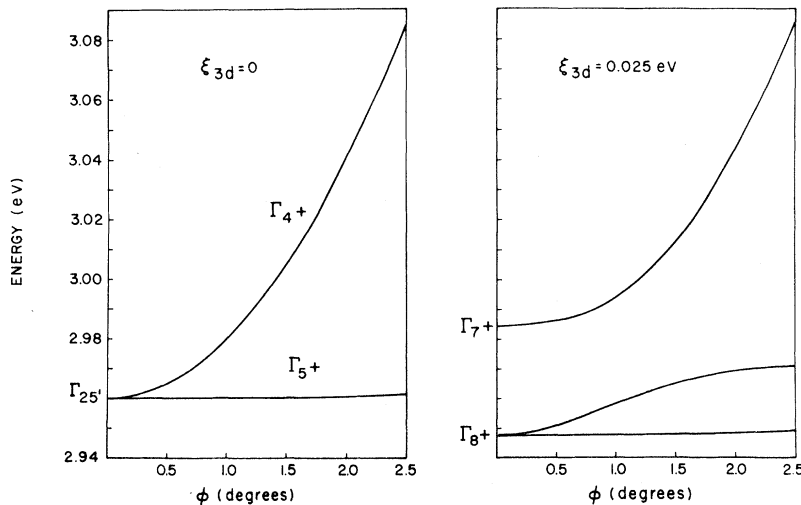


FIG. 3. Splitting of the SrTiO₃ conduction-band minimum as a function of the rotation angle ϕ with $\xi_{3d}=0$ and $\xi_{3d}=0.025$ eV.

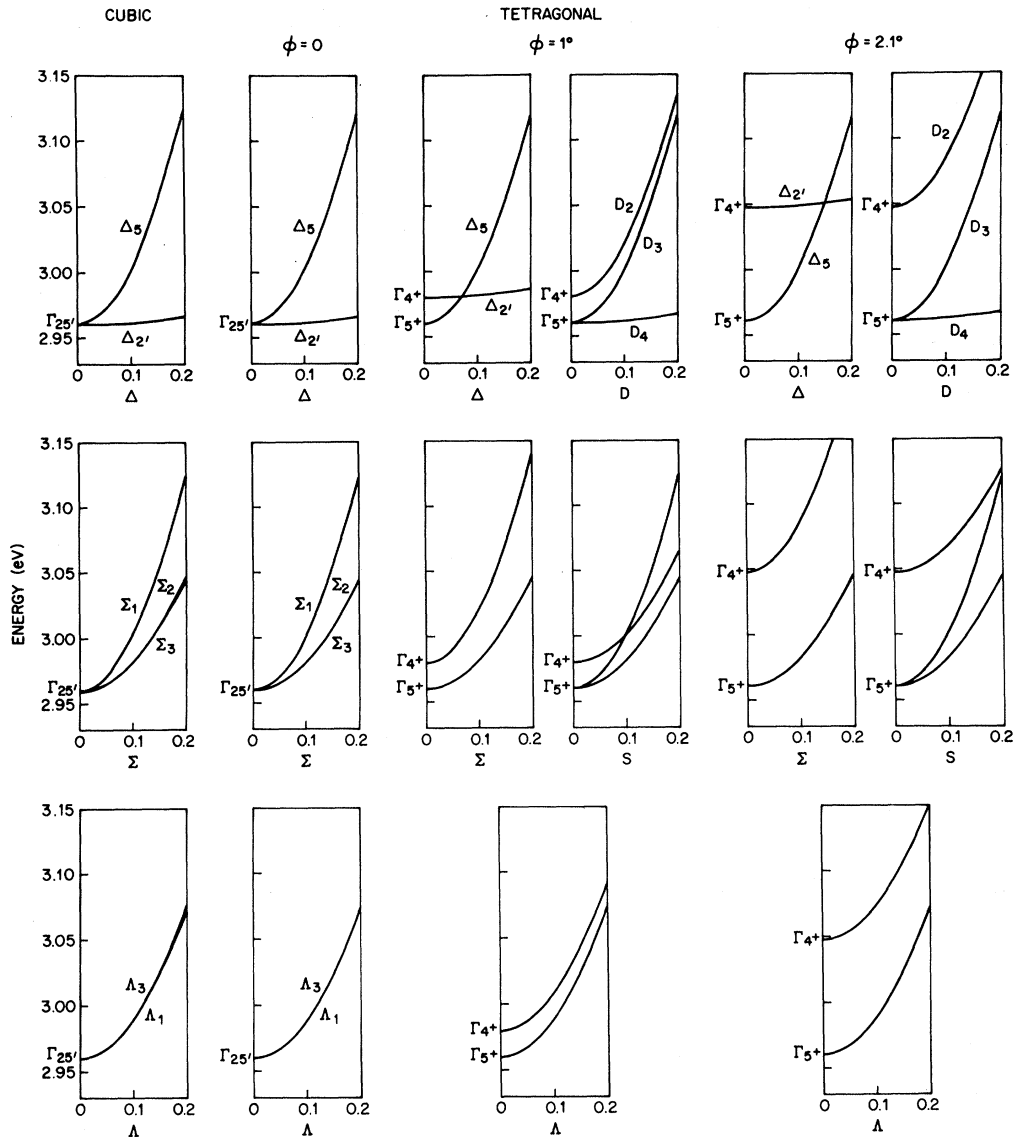


FIG. 4. $E(\vec{k})$ along symmetry directions for $\varphi=0, 1^\circ$, and 2.1° . The results in the first column are obtained from the cubic LCAO model of I. Wave-vector magnitudes are in units of (π/a) .

band crossings in most symmetry directions. However, most of the qualitative features of the results shown in Fig. 4 are preserved in Fig. 5, including the flat band along the D direction.

It is clear from the results of Fig. 5 that the tetragonal distortion has an important effect on the shape of the constant-energy surfaces in n -type SrTiO_3 . The bulges that exist along all three $\langle 100 \rangle$ directions in the cubic state occur only along the $[100]$ and $[010]$ directions in the tetragonal state. This is illustrated in Fig. 6, where constant-energy surfaces for cubic ($\varphi=0$) and tetragonal ($\varphi=2.1^\circ$) SrTiO_3 are compared. In both cases, these surfaces correspond to Fermi energies (relative to

the band edge) of 12.7, 16.7, and 20.7 meV. The results for the tetragonal state represent carrier densities $n=0.8, 1.5,$ and $2.5 \times 10^{19} \text{ cm}^{-3}$. For $\varphi=2.1^\circ$ and $\xi_{3d}=0.025 \text{ eV}$, the splitting of the lowest pair of bands at Γ is 20.7 meV, so that the second band is occupied in the tetragonal state for $n > 2.5 \times 10^{19} \text{ cm}^{-3}$.

In I, we designated the carriers that are associated with the inner (dashed) and outer (solid) constant-energy surfaces in cubic n -type SrTiO_3 as "light" and "heavy" electrons, respectively. According to Figs. 5 and 6, the bands associated with light electrons in tetragonal SrTiO_3 are unoccupied at low carrier densities. It is clear that the

cubic-to-tetragonal structural transformation has little effect on the shape of the constant-energy surface for the heavy electrons in the plane perpendicular to the c axis. However, the prominent bulges that exist along $[001]$ or the c axis of the heavy-electron surface are removed in the tetragonal state.

For Fermi energies greater than 20.7 meV, two bands are occupied. The shape of the constant-energy surface for $E_F = 40$ meV is shown in Fig. 7, where $n = n_l + n_h = 1.12 \times 10^{20} \text{ cm}^{-3}$. At this energy, the ratio $n_l/n_h = 0.086$.

Cyclotron masses have been calculated for orbits on the tetragonal SrTiO_3 constant-energy sur-

faces with the magnetic field \vec{H} in various symmetry planes. These results are shown in Fig. 8 for the three carrier densities shown in Fig. 6. In agreement with the results of similar calculations for cubic SrTiO_3 in I, it is found that the cyclotron-mass results for tetragonal SrTiO_3 depend on the carrier density, particularly for orbits which pass near the $[100]$ and $[010]$ bulges. Similar results have been obtained for the constant-energy surface shown in Fig. 7. In this case, the mass ratios for light (heavy) electrons with \vec{H} along $[001]$, $[100]$, and $[110]$ are 0.83, 0.67, 0.83 (6.0, 3.5, 0.8), respectively. The cyclotron-mass results for the heavy electrons are consid-

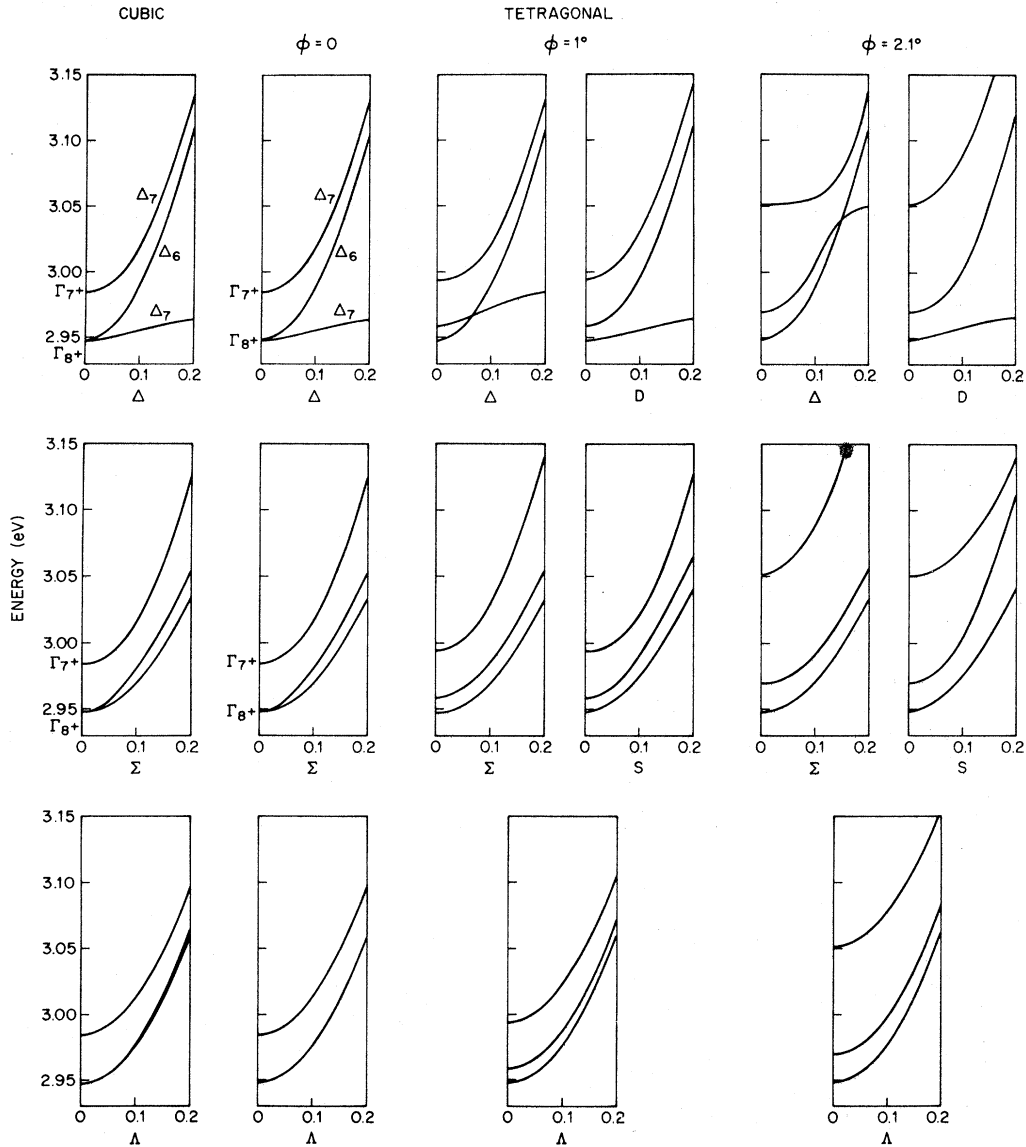


FIG. 5. $E(\vec{k})$ curves for tetragonal SrTiO_3 , including the effects of spin-orbit coupling with $\xi_{3d} = 0.025$ eV.

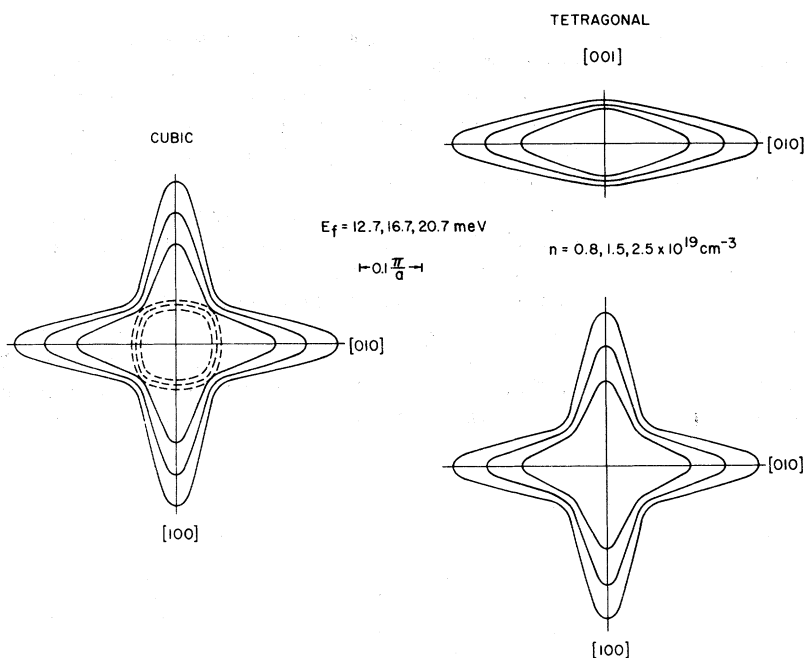


FIG. 6. Constant-energy surfaces for cubic ($\varphi = 0$) and tetragonal ($\varphi = 2.1^\circ$) SrTiO_3 .

erably less accurate at these high carrier densities because the constant-energy surfaces become grossly anisotropic in shape.

V. DISCUSSION

The results of Sec. IV predict that the 110 ° K cubic-to-tetragonal phase transition produces large changes in the SrTiO_3 conduction bands, effects which should be observable in monodomain samples at low temperatures. The present analysis is concerned entirely with the band-structure changes that are caused by the cubic-to-tetragonal structural transformation. No attempt has been made to estimate the additional modifications that may result from the other low-temperature phase transitions that are suggested by the data of Lytle³ and Sakudo and Unoki.⁵

Despite the large number of experimental studies that have been performed on pure and doped SrTiO_3 samples, many gaps still remain in our over-all knowledge of its low-temperature properties. One question of primary importance concerns the effects of doping on the intrinsic properties of pure SrTiO_3 . The results of several different experiments suggest that fundamental differences may exist between the properties of self-doped (oxygen-deficient) and Nb-doped samples of SrTiO_3 . For example, ultrasonic measurements by Jones and co-workers²⁰ show that the cubic-to-tetragonal phase transition that is observed in insulating SrTiO_3 samples at 110 ° K is depressed to 85 ° K for self-doped samples but is unchanged for Nb-doped samples with the same

carrier density ($n \sim 10^{20} \text{ cm}^{-3}$). Similarly, in their electron-spin-resonance studies of Fe^{3+} in SrTiO_3 , Unoki and Sakudo⁴ find that the observed angle of distortion φ is reduced by 30% if the immediate

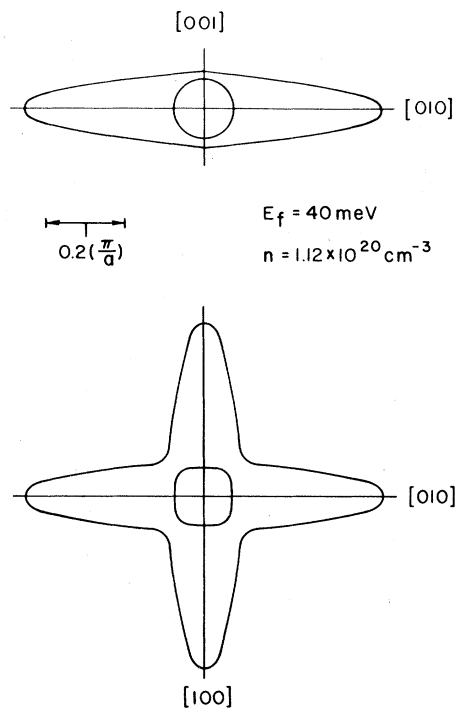


FIG. 7. Constant-energy surfaces for tetragonal SrTiO_3 for $n = 1.12 \times 10^{20} \text{ cm}^{-3}$.

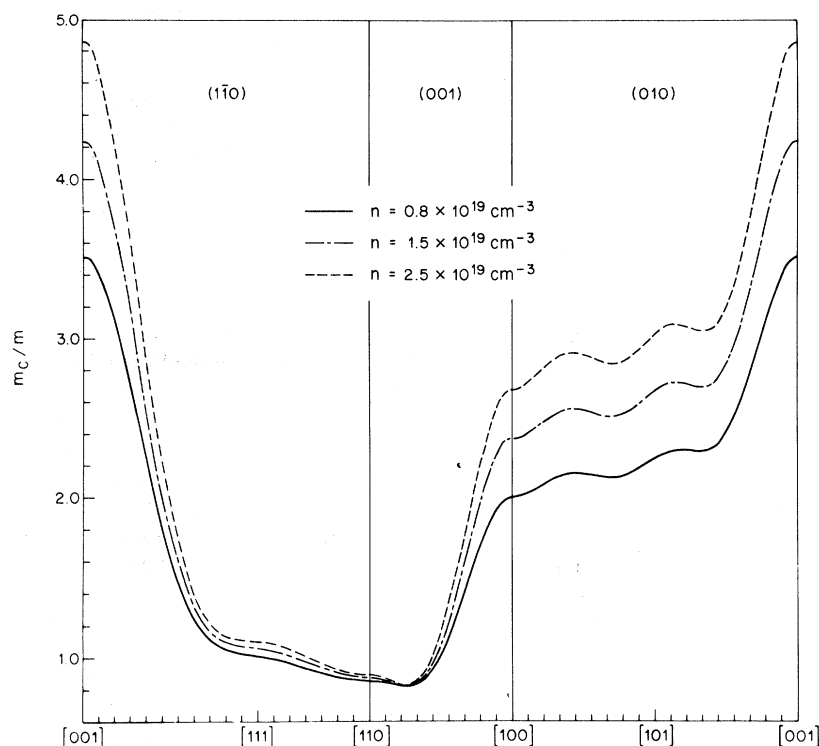


FIG. 8. Cyclotron-mass results for n -type tetragonal SrTiO_3 .

environment of an Fe^{3+} ion includes a nearest-neighbor oxygen vacancy. These results suggest that the magnitude of the low-temperature distortion may be reduced significantly in the self-doped samples.

These differences between the self-doped and Nb-doped samples are also reflected in the low-temperature heat-capacity results of Phillips *et al.*¹¹ These data indicate that the self-doped SrTiO_3 samples contain a significant concentration of paramagnetic centers, which Phillips *et al.*²¹ attribute to localized Ti^{3+} ions that are trapped between pairs of oxygen vacancies. They find that the concentration of these paramagnetic centers increases with the carrier density n in the self-doped materials²¹ and is about ten times larger in the self-doped materials than in Nb-doped samples of comparable carrier density.¹¹

Phillips *et al.*¹¹ also note that uncertainties exist in the values for the density of states that are inferred from heat-capacity data for both the self-doped and Nb-doped samples of SrTiO_3 . In both cases, they observe that the data exhibit deviations from the temperature dependence that is expected for the sum of lattice and electronic heat capacities. In addition to a term associated with paramagnetic centers, they also find that the heat capacity includes a possible contribution from the low-temperature structural transformations. In view of these uncertainties, it is perhaps not

surprising that the agreement between the experimental and calculated density-of-states (DS) results for n -type SrTiO_3 is relatively poor. In Fig. 9, we compare the DS results that are derived from the heat-capacity data of Phillips *et al.*¹¹ and Ambler *et al.*²² with the calculated band-density-of-states results. In general, the "experimental" values for the density of states are 3–5

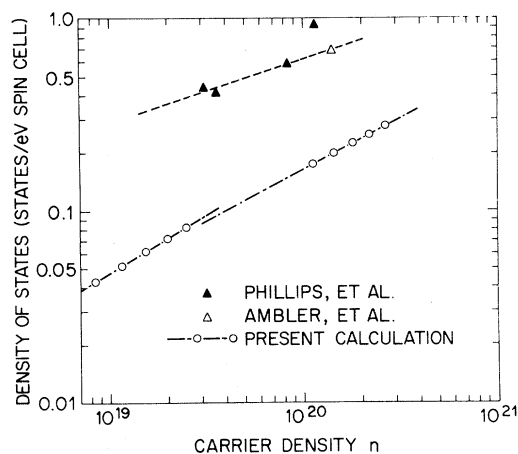


FIG. 9. Comparisons between experimental heat capacity and calculated DS results for n -type SrTiO_3 . The dashed line through the experimental data represents an $n^{1/3}$ dependence.

times larger than the calculated values. It is found that the experimental values for γ (and the corresponding values for the density of states) are roughly proportional to $n^{1/3}$. However, non-parabolic effects cause a more rapid increase in the calculated dependence of the density of states on n .

The results of low-temperature piezoresistance studies on n -type SrTiO₃ samples indicate an anisotropy in the electrical resistivity which is consistent with the mass anisotropy that is predicted by the present LCAO model for the conduction bands in the tetragonal state. Tufte and Stelzer⁶ and Frederikse *et al.*⁷ have studied the piezoresistive properties of self-doped and Nb-doped samples at low temperatures. Below 110 °K, they observe that the resistivity increases if a compressive stress is applied along a [001] axis and decreases for tensile stress. They observe a saturation of the piezoresistive effect at low stress values of $1-2 \times 10^8$ dyn/cm². This is the same stress range where Müller *et al.*¹² have shown that a uniaxial compressional stress along a [001] axis will flip 85–90% of the domains so their c axes are perpendicular to the stress direction. Presumably, tensile stress produces a monodomain sample with the c axis aligned parallel to the stress direction. For a Nb-doped sample with $n = 6 \times 10^{18}$ cm⁻³, Frederikse *et al.*⁷ find a 10% increase in the resistivity for compressional stress and a 10% decrease for tensile stress. If these changes are attributed entirely to the alignment of domains perpendicular and parallel to the stress axis, then these results suggest that the resistivity along the c axis is 20% smaller than that in the basal plane. This is consistent with the results of the present calculations which show that the cubic-to-tetragonal structural transformation causes a decrease in mass for electrons with wave vectors along or near the c axis but not in the basal plane.

It is interesting to contrast the resistance anisotropy in tetragonal SrTiO₃ with that observed in ferroelectric BaTiO₃. At room temperature, Berglund and Baer¹⁹ find that the resistivity parallel to the c axis is ten times greater than that in a perpendicular direction. Thus, the resistivity anisotropy in ferroelectric BaTiO₃ is much larger in magnitude and opposite in sign to that observed in tetragonal SrTiO₃. In both cases, however, the sign of the effect is consistent with the prediction that the masses in the tetragonal state are reduced for electrons whose wave vectors point along directions which are parallel (SrTiO₃) and perpendicular (BaTiO₃) to the c axis, respectively.

By the use of monodomain samples, it may be possible to perform a decisive experiment which can distinguish between the warped-band and

many-valley models for the conduction bands of tetragonal SrTiO₃. The two most promising experimental techniques for such a study are cyclotron resonance and the Shubnikov-de Haas effect. The latter experiment is particularly attractive since Frederikse *et al.*²³ have already observed Shubnikov-de Haas oscillations in SrTiO₃ samples which were presumably multidomain in character. Using a monodomain sample, a systematic study of the Shubnikov-de Haas frequency variation in one or more symmetry planes could probably distinguish between the present warped-band and Kahn-Leyendecker² many-valley models for the SrTiO₃ conduction bands. By extending the present analysis to the many-valley model, it is clear that the tetragonal distortion will empty the valley along the c axis, leaving two ellipsoids centered at the X points in the basal plane (see Fig. 2) with their major axes along the [100] and [010] directions, respectively. According to the results shown in Figs. 6 and 7, the warped-band model for tetragonal SrTiO₃ yields constant-energy surfaces that are essentially the sum of two such ellipsoids, both centered at Γ . The uncrossing of bands separates these overlapping ellipsoids into the light- and heavy-electron surfaces, and only the latter is expected to be occupied at low carrier densities.

To varying degrees, the effects of the cubic-to-tetragonal phase transition have manifest themselves in other experimental data. Frederikse *et al.*⁸ observe 10% changes in the magnetoresistance of a sample when it is warmed to room temperature and then recooled. These changes are attributed to shifting domain patterns. Similar effects have been observed by Tufte and Stelzer⁹ in their low-temperature data.

Blazey¹⁰ has studied the temperature-dependence of the wavelength-modulated absorption and reflectivity spectra of SrTiO₃ near the band gap. He attributes a peak in the reflectivity spectrum at 3.34 eV to the lowest energy direct band gap. He also observes structure in the absorption at lower energies, which he interprets as indirect transitions. Between 100 and 140 °K, Blazey observes two minima in the absorption which are separated by about 30 meV; he attributes these two minima to the coexistence of the cubic and tetragonal phases over this temperature range. However, Redfield and Burke²⁴ have suggested an alternative interpretation of these data which involves phonon emission and absorption and does not require the coexistence of the cubic and tetragonal phases near the 110 °K structural transformation.

As discussed in I, the present calculations for cubic SrTiO₃ predict that the band gap is direct. It is found that both the conduction-band minimum and the valence-band maximum occur at the zone

center. However, the location of the valence-band maximum is not a particularly reliable result since similar calculations for KNiF_3 , KMoO_3 , and ReO_3 predict that this maximum occurs at either the M or R points in the Brillouin zone. Since Γ and R become equivalent in the tetragonal state, the valence-band maximum must occur at either X or M if the edge is to remain indirect in both the cubic and tetragonal states. It is possible that the location of the valence-band maximum is shifted by band-structure changes that are caused by the tetragonal distortion, as suggested previously by Fleury *et al.*¹⁴ Since the present LCAO model for tetragonal SrTiO_3 contains an oversimplified treatment of the oxygen- $2p$ valence bands, it provides little information about these effects.

It is interesting to compare the optical dichroism that is observed in tetragonal SrTiO_3 and BaTiO_3 . Wemple²⁵ finds that at 23 °C, the two Urbach edges corresponding to light polarized parallel (α_{\parallel}) and perpendicular (α_{\perp}) to the c axis are separated by 108 meV, with $\alpha_{\perp} > \alpha_{\parallel}$ at a given photon energy. This splitting is quite similar in magnitude to the 120 meV splitting of the BaTiO_3 conduction band that Berglund and Baer¹⁹ infer from their Seebeck measurements. This suggests that the dichroism of 108 meV arises primarily from the splitting of the conduction-band minimum in the ferroelectric state. Although the present calculations predict a comparable splitting of the SrTiO_3 conduction-band edge in the tetragonal state, Müller *et al.*¹² and Capizzi and Frova²⁶ report a 3 meV dichroism in tetragonal SrTiO_3 at 82 °K. They observe that the dichroism is opposite in sign ($\alpha_{\parallel} > \alpha_{\perp}$) to that observed by Wemple in BaTiO_3 and smaller in magnitude. In terms of the present results, this suggests that the origin of the dichroism in tetragonal SrTiO_3 may be more complicated than that in BaTiO_3 and may involve changes in both the SrTiO_3 valence- and conduction-band states.

Superconductivity has been observed in self-doped and Nb-doped samples of SrTiO_3 with carrier densities in the 8×10^{18} to $3 \times 10^{20} \text{ cm}^{-3}$ range.²⁷ The transition temperature T_c falls to zero at the lower and upper carrier-density limits and reaches a maximum of about 0.3 °K near $n = 8 \times 10^{19} \text{ cm}^{-3}$. Phillips *et al.*¹¹ note that the T_c -vs- n behavior appears to be different for the self-doped and Nb-doped samples. They observe that the Nb-doped samples tend to have higher T_c 's, and there is no well-defined maximum in the T_c -vs- n curve for

these samples. They suggest that the decrease in T_c with increasing n may be a consequence of the increasing concentration of paramagnetic centers in the self-doped materials.²¹

Several theories have been proposed to explain the observed variation in T_c as a function of n . Each neglects the possible influence of paramagnetic centers on T_c in the high carrier-density limit. The theory proposed by Cohen²⁸ emphasizes the importance of intervalley phonons in explaining the occurrence of superconductivity in many-valley semiconductors and semimetals. Koonce *et al.*²⁷ have applied this theory to SrTiO_3 , assuming a many-valley model for the conduction bands which is based on the Kahn-Leyendecker calculation.² The theory of Appel²⁹ emphasizes the intravalley exchange of soft optical phonons between conduction electrons, whereas the small-polaron theory of Zinamon³⁰ involves intravalley acoustic-phonon interactions. Each of these theories provides an accurate representation of the observed dependence of T_c on n . However, the latter two models appear to be more consistent with the present model for the SrTiO_3 conduction bands since they involve only intravalley phonon processes.

Pfeiffer and Schooley³¹ have studied the effect of stress on T_c in both self-doped and Nb-doped samples. They find that T_c is generally reduced by hydrostatic pressure or uniaxial compression. However, they do observe that T_c increases for [100] compression in a Nb-doped sample and decreases for a similar compression in a self-doped sample. These results provide additional evidence for suspecting a fundamental difference between the Nb-doped and self-doped samples. The interpretation of these data is also complicated by the fact that Burke and Pressley³² observe a stress-induced ferroelectric transition in insulating SrTiO_3 samples in this stress range.

It should be clear from this discussion that many experimental uncertainties remain regarding the low-temperature band structure of SrTiO_3 . Hopefully, the results of the present calculations will stimulate new experimental studies which will help eliminate some of these ambiguities.

ACKNOWLEDGMENTS

I would like to acknowledge helpful conversations with P. B. Allen, J. R. Brews, P. A. Fleury, L. R. Testardi, and S. H. Wemple on various aspects of this investigation.

¹L. F. Mattheiss, preceding paper, Phys. Rev. B **6**, 4718 (1972).

²A. H. Kahn and A. J. Leyendecker, Phys. Rev. **135**, A1321 (1964).

³F. W. Lytle, J. Appl. Phys. **35**, 2212 (1964).

⁴H. Unoki and T. Sakudo, J. Phys. Soc. Japan **23**,

546 (1967).

⁵T. Sakudo and H. Unoki, Phys. Rev. Letters **26**, 851 (1971).

⁶O. N. Tufte and E. L. Stelzer, Phys. Rev. **141**, 675 (1966).

⁷H. P. R. Frederikse, W. R. Hosler, and R. C.

Casella, in *Proceedings of the Ninth International Conference on the Physics of Semiconductors*, edited by S. M. Ryukin (Nauka, Leningrad, 1968).

⁸H. P. R. Frederikse, W. R. Hosler, and W. R. Thurber, *Phys. Rev.* **143**, 648 (1966).

⁹O. N. Tufte and E. L. Stelzer, *Phys. Rev.* **173**, 775 (1968).

¹⁰K. W. Blazey, *Phys. Rev. Letters* **27**, 146 (1971).

¹¹N. E. Phillips, B. B. Triplett, R. D. Clear, H. E. Simon, J. K. Hulm, C. K. Jones, and R. Mazelsky, in *Proceedings of the International Conference on the Science of Superconductivity*, edited by F. Chilton (North-Holland, Amsterdam, 1971).

¹²K. A. Müller, W. Berlinger, M. Capizzi, and H. Gränicher, *Solid State Commun.* **8**, 549 (1970).

¹³G. F. Koster, in *Solid State Physics*, edited by F. Seitz and D. Turnbull (Academic, New York, 1957).

¹⁴P. A. Fleury, J. F. Scott, and J. M. Worlock, *Phys. Rev. Letters* **21**, 16 (1968).

¹⁵G. Shirane and Y. Yamada, *Phys. Rev.* **177**, 858 (1969); R. A. Cowley, W. J. L. Buyers, and G. Dolling, *Solid State Commun.* **7**, 181 (1969).

¹⁶J. R. Brews, *Phys. Rev. Letters* **18**, 662 (1967).

¹⁷B. C. Frazer, H. R. Danner, and R. Pepinsky, *Phys. Rev.* **100**, 745 (1955).

¹⁸J. D. Zook and T. N. Casselman, *Phys. Rev. Letters* **17**, 960 (1966).

¹⁹C. N. Berglund and W. S. Baer, *Phys. Rev.* **157**,

358 (1967).

²⁰C. K. Jones and J. K. Hulm, *Phys. Letters* **26A**, 182 (1968); D. W. Deis, J. K. Hulm, and C. K. Jones, *Bull. Am. Phys. Soc.* **14**, 61 (1969); D. W. Deis, M. Ashkin, J. K. Hulm, and C. K. Jones, *ibid.* **15**, 102 (1970).

²¹N. E. Phillips, J. C. Ho, D. P. Woody, J. K. Hulm, and C. K. Jones, *Phys. Letters* **29A**, 356 (1969).

²²E. Ambler, J. H. Colwell, W. R. Hosler, and J. F. Schooley, *Phys. Rev.* **148**, 280 (1966).

²³H. P. R. Frederikse, W. R. Hosler, W. R. Thurber, J. Babiskin, and P. G. Siebenmann, *Phys. Rev.* **158**, 775 (1967).

²⁴D. Redfield and W. J. Burke, *Phys. Rev. Letters* **28**, 435 (1972).

²⁵S. H. Wemple, *Phys. Rev. B* **2**, 2679 (1970).

²⁶M. Capizzi and A. Frova, *Nuovo Cimento* **5B**, 181 (1971).

²⁷C. S. Koonce, M. L. Cohen, J. F. Schooley, W. R. Hosler, and E. R. Pfeiffer, *Phys. Rev.* **163**, 380 (1967).

²⁸M. L. Cohen, *Phys. Rev.* **134**, A511 (1964).

²⁹J. Appel, *Phys. Rev.* **180**, 508 (1969).

³⁰Z. Zinamon, *Phil. Mag.* **21**, 347 (1970).

³¹E. R. Pfeiffer and J. F. Schooley, *J. Low Temp. Phys.* **2**, 333 (1970).

³²W. J. Burke and R. J. Pressley, *Solid State Commun.* **9**, 191 (1971).

Raman Scattering, Luminescence, and Exciton-Phonon Coupling in Cu_2O [†]

A. Compaan and H. Z. Cummins*

Department of Physics, New York University, New York, New York 10003

(Received 29 June 1972)

Raman scattering and exciton luminescence and absorption have been studied in high-purity single-crystal Cu_2O at liquid-helium temperature using 4880-Å laser excitation. The Raman-active mode has been unambiguously identified at 515 cm^{-1} , and the first observation made of luminescence from the $n=2, 3, 4$ yellow excitons and their continuum. Comparison of the Raman spectra with the absorption and luminescence spectra near the $n=1$ exciton has clarified the origin of the strong 220- cm^{-1} Raman feature and yielded evidence for wave-vector-independent and wave-vector-dependent exciton-phonon coupling, respectively, for the Γ_{12}^- and Γ_{15}^- optic phonons.

INTRODUCTION

In this paper we present the results of Raman scattering and laser-excited recombination luminescence from the yellow exciton series¹⁻³ in cuprous oxide Cu_2O . These measurements have allowed us to unambiguously identify at 515 cm^{-1} the Γ_{25}^+ Raman-active mode whose frequency has previously been reported as 220, 197, and 598 cm^{-1} by various groups.⁴⁻⁶ We have also observed for the first time the direct recombination radiation from the $n=2, 3, 4$ and higher exciton states and from the series continuum. Comparison of the Raman spectra with the phonon-assisted 1S exci-

ton luminescence has clarified the origin of other features of the Raman spectrum, such as the strongest peak at 220 cm^{-1} which we identify as scattering from two 110- cm^{-1} phonons. Finally, digital measurements of phonon-assisted 1S exciton absorption have indicated that the exciton-phonon coupling is independent of the phonon wave vector q for the Γ_{12}^- phonon but linear in q for the Γ_{15}^- phonon.

Our experiments were performed on a 1-mm-thick slice from a large single-crystal Cu_2O boule grown by Brower and Parker⁷ by a floating-zone technique. Forman, who has studied the optical absorption of these crystals,⁸ provided